Materials Chemistry and Physics 319 (2024) 129230

Contents lists available at ScienceDirect

Materials Chemistry and Physics

journal homepage: www.elsevier.com/locate/matchemphys

Characterization of the magnetocaloric effect in RMn_6Sn_6 including high-entropy forms

Kyle Fruhling *, Xiaohan Yao, Alenna Streeter, Fazel Tafti

Department of Physics, Boston College, Chestnut Hill, MA 02467, USA

HIGHLIGHTS

- The magnetocaloric effect in RMn_6Sn_6 depends sensitively on the rare-earth.
- RMn_6Sn_6 family is a tunable platform to study high temperature MCE.
- High-entropy forms are not always a viable path to increase MCE.

ARTICLE INFO

Keywords:
Magnetocaloric effect
Kagome lattice
Rare-earth

ABSTRACT

We present a comprehensive study of the magnetocaloric effect (MCE) in a family of kagome magnets with formula RMn_6Sn_6 (R=Tb, Ho, Er, and Lu). These materials have a small rare-earth content and tunable magnetic ordering, hence they provide a venue to study the fundamentals of the MCE. We examine the effect of different types of order (ferrimagnetic and antiferromagnetic) and the presence of a metamagnetic transition on the MCE. We extend the study to the high-entropy rare-earth forms of the RMn_6Sn_6 family. Our results suggest several guidelines for enhancing the MCE in tunable magnetic materials with small rare-earth content.

1. Introduction

Since the discovery of a giant magnetocaloric effect (MCE) in $Gd_5Si_2Ge_2$ by Pecharsky and Gschneidner [1], magnetic refrigeration has been considered as a viable replacement for conventional gas refrigeration. Engineering designs already exist for magnetic refrigerators that are at least 20% more energy efficient than gas refrigerators [2,3]. The higher energy efficiency as well as the elimination of greenhouse and ozone-depleting gases make magnetic refrigeration a critical aspect of sustainability. However, there are several challenges related to magnetocaloric materials (MCMs) that must be addressed before magnetic refrigerators can be commercialized. (i) Current benchmark MCMs are either elemental Gd and Ho or rare-earth-rich compounds such as $Gd_5Si_2Ge_2$, and HoB_2 [4–7]. Since using large amounts of rare-earth is not sustainable, attempts have been made to find rare-earth-light or rare-earth-free MCMs. Some of the most successful MCMs have been rare-earth-light such as Gd_2MgTiO_6, R_2BaZnO_5 and $GdFe_2Si_2$ [8–10]. However, these materials have transition temperatures below 10 K making them useful for cryogenic applications, but not everyday refrigeration. Rare-earth-free MCMs such as $AlFe_2B_2$ and MnAs have also been investigated [11–13]. Unfortunately, these materials are either less efficient or contain toxic elements such as As and P. (ii) The giant MCE in rare-earth-rich materials originates from a large entropy release in a narrow temperature range across a first-order magneto-structural phase transition (FOPT). The hysteresis in a FOPT limits thermal cycling of the material. (iii) Recently, disorder has been used to broaden the magnetic transition and enhance the refrigerant capacity in Heusler compounds and high-entropy alloys [14–16]. In MnCoGe for example, alloying at the Mn site with Cu to make $Mn_{0.9}Cu_{0.1}CoGe$ increases the maximum magnetic entropy change sixfold [17]. However, disorder works against the structural integrity of MCMs and is a challenging parameter to control during manufacturing processes. (iv) Few microscopic mechanisms besides FOPT and disorder have been proposed to improve the MCE. A poor theoretical understanding of the microscopic mechanisms that control the MCE severely limits the pace of discovering high-efficiency MCMs.

In this work, we use a tunable family of RMn_6Sn_6 materials (R=Tb, Ho, Er, and Lu) to provide the groundwork to gain a deeper insight into the fundamentals of the MCE. The magnetic properties of RMn_6Sn_6 systems have been reported in prior publications [18–20] but not in a comparative manner. Particularly, there has been no comparison between the MCE of these compounds. Here we present such a comparative study and add the MCE for high-entropy forms of RMn_6Sn_6, which have not been studied in any prior works.

* Corresponding author.
E-mail address: fruhling@bc.edu (K. Fruhling).

https://doi.org/10.1016/j.matchemphys.2024.129230
Received 23 January 2024; Received in revised form 12 March 2024; Accepted 21 March 2024
Available online 27 March 2024

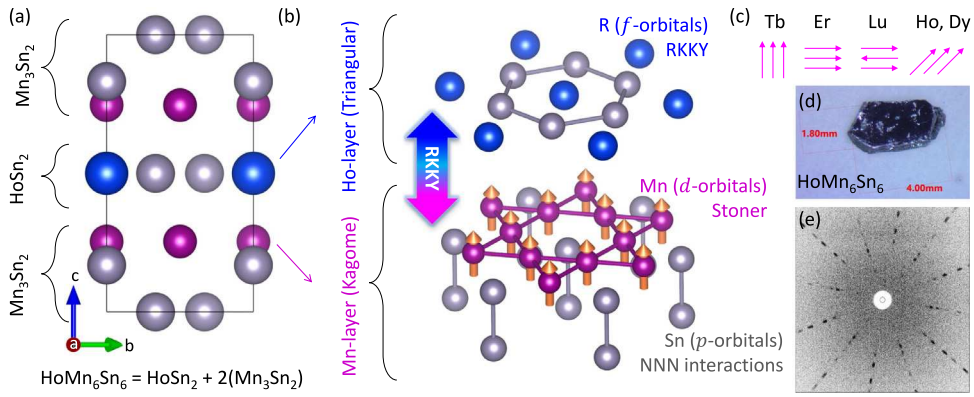

Fig. 1. (a) Each unit cell of $HoMn_6Sn_6$ (a representative member of RMn_6Sn_6 family) contains one triangular layer of $HoSn_2$ sandwiched between two kagome layers of Mn_3Sn_2. (b) The electronic structure consists of itinerant p and d electrons as well as localized f electrons provided by Sn, Mn, and Ho, respectively. (c) Magnetism in the Mn layers varies significantly by changing the rare-earth due to RKKY interactions. (d) Optical image of a large single crystal. (e) Laue diffraction along the crystallographic c-axis confirms the hexagonal unit cell ($P6/mmm$) and absence of twinning in the crystal.

Each unit cell of RMn_6Sn_6 comprises one layer of RSn_2 sandwiched between two layers of Mn_3Sn_2 (Figs. 1a, b). The manganese atoms form a kagome lattice and rare-earth atoms form a triangular lattice. Only 1 out of 13 atoms in the chemical formula is a lanthanide. The small rare-earth content (<8%) and absence of toxic elements in the composition make these materials a sustainable platform for the MCE.

The RMn_6Sn_6 system hosts a variety of magnetic structures (Fig. 1c) due to Ruderman–Kittel–Kasuya–Yosida (RKKY) interactions between the itinerant electrons (Mn-d and Sn-p electrons) and local moments (rare-earth f electrons) [21,22]. Magnetism can be easily tuned from ferrimagnetic (FIM) to antiferromagnetic (AFM) by changing the rare-earth element as illustrated in Fig. 1c. The magnitude of the MCE in RMn_6Sn_6 presented here is not larger than the recent rare-earth-free magnetocaloric materials [23–25], as expected from a system with small rare-earth content. However, the RMn_6Sn_6 family offers tunable magnetism due to RKKY interactions, which is not accessible in rare-earth-free systems. We study the effect of different magnetic structures on the MCE by comparing the magnetic entropy change (ΔS_m), full width at half maximum (FWHM) of $-\Delta S_m$, and refrigerant capacity (RC) across the high-temperature magnetic transition of $TbMn_6Sn_6$, $HoMn_6Sn_6$, $ErMn_6Sn_6$, and $LuMn_6Sn_6$.

Following the work of Yeh et al. in the early 2000s [26], high-entropy alloys (HEAs) have been used in applications that require extreme strength, oxidation resistance, and high-temperature stability [27]. Recently, HEAs of transition-metals, such as MnFeCoNiCu and $(FeCoNi)_{60}Cu_{19}Mn_{21}$, have shown a notable magnetocaloric performance [28–30]. For this reason, we also investigate the MCE of a high-entropy form (HEF) of RMn_6Sn_6. Interestingly, we find the MCE in the HEF of RMn_6Sn_6 is comparable to and slightly larger than some transition metal high-entropy alloys [31,32].

2. Experimental methods

2.1. Material synthesis

Single crystals of RMn_6Sn_6 were grown using a self-flux technique. The starting chemicals were terbium, holmium, erbium, and lutetium pieces (99.9%), manganese granules (99.98%), and tin pieces (99.999%). They were mixed with the ratio R:Mn:Sn = X:6:18 (X = 1.25 for Tb, 1.50 for Ho, 1.10 for Er, and 1.20 for Lu), placed in alumina crucibles and sealed inside evacuated silica tubes. The tubes were heated in a box furnace to 1000 °C at 3 °C/min, held at that temperature for 12 h, cooled to 600 °C at 6 °C/h, and centrifuged to remove the excess flux. Using lesser amounts of rare-earth or centrifuging at T < 600 °C resulted in the formation of impurity phases such as $HoSn_2$ and $RMnSn_2$.

The crystallographic structure was verified by Laue X-ray diffraction using a real-time back-reflection MWL120 system. Picture of a representative $HoMn_6Sn_6$ crystal and its Laue diffraction pattern are shown in Figs. 1d, e. The chemical composition of each material was confirmed by energy dispersive X-ray spectroscopy (EDX) in an FEI Scios DualBeam electron microscope equipped with Oxford detector. The EDX spectra and composition analyses of RMn_6Sn_6 samples are presented in the supplemental Fig. S1 and Table. S1.

2.2. Magnetic measurements

Magnetization measurements were performed on single crystals using a 7 T Quantum Design MPMS-3 equipped with vibrating sample magnetometry (VSM) and oven options. The MCE was quantified by measuring magnetization isotherms in the vicinity of the critical temperature and evaluating the magnetic entropy change (ΔS_m) using the Maxwell equation [33,34],

$$\Delta S_m(T, \Delta H) = \int_0^{H_{max}} \left(\frac{\partial M}{\partial T}\right)_H dH \quad (1)$$

which was approximated with the following expression for discrete isotherms:

$$\Delta S_m\left(T = \frac{T_1 + T_2}{2}\right) = \left(\frac{1}{T_2 - T_1}\right) \times \left[\int_0^{H_{max}} M(T_2, H)\, dH - \int_0^{H_{max}} M(T_1, H)\, dH\right] \quad (2)$$

using H_{max} = 0.5, 2, and 5 T. A bell-shaped curve was obtained for $-\Delta S_m(T)$ with three parameters that characterize the MCE: (i) the height of the curve ($-\Delta S_{MAX}$), (ii) full width at half maximum (FWHM), and (iii) refrigerant capacity (RC) defined as the area under the curve.

$$RC = \int_{FWHM} -\Delta S_m(T)\, dT \quad (3)$$

In this article, we will focus on the MCE in the vicinity of the highest temperature magnetic transition in each RMn_6Sn_6 compound. However, these compounds also have one or two low-temperature transitions. We present the low-temperature MCE as supplemental material (Fig. S2) since it is not relevant for technological applications.

3. Results and discussion

3.1. Temperature dependence of magnetic susceptibility

The magnetic ordering of RMn_6Sn_6 depends sensitively on the choice of rare-earth element, evidence of a strong R-Mn coupling due

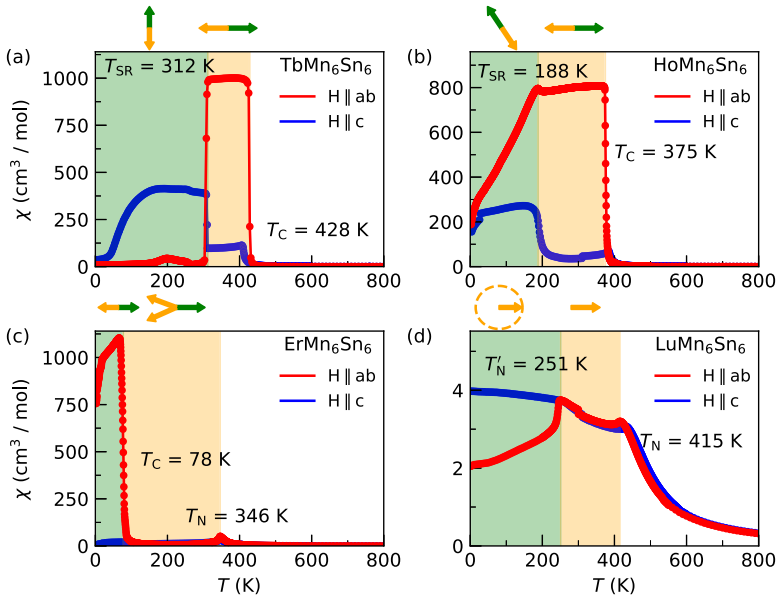

Fig. 2. Temperature dependence of the zero-field cooled magnetic susceptibility in (a) $TbMn_6Sn_6$, (b) $HoMn_6Sn_6$, and (c) $ErMn_6Sn_6$ measured at $\mu_0 H$ = 100 Oe, and (d) $LuMn_6Sn_6$ measured at $\mu_0 H$ = 5000 Oe. The green arrows represent the direction of the rare-earth moment and the orange arrows represent the direction of the Mn moment. (For interpretation of the references to color in this figure legend, the reader is referred to the web version of this article.)

to RKKY interactions. Fig. 2 shows temperature dependence of the magnetic susceptibility $\chi(T)$ in RMn_6Sn_6 for R=Tb, Ho, Er, and Lu with $H \parallel ab$ and with $H \parallel c$. All four compounds undergo different magnetic transitions at high (T > 300K) and low (T < 300K) temperatures. In each case, the rare-earth and Mn moments, represented by the green and orange arrows respectively, are antiparallel. In Fig. 2a, $TbMn_6Sn_6$ shows an FIM transition with in-plane moments at the Curie temperature T_C=428 K. It then undergoes a spin reorientation at T_{SR}=312 K where the moments rotate from in-plane to out-of-plane direction as confirmed by the susceptibility measurements with $H \parallel c$. In Fig. 2b, $HoMn_6Sn_6$ shows an in-plane FIM transition at T_C=375 K and a spin reorientation transition at T_{SR}=188 K where the moments cant towards the c-axis [35,36]. In Fig. 2c, $ErMn_6Sn_6$ shows an AFM transition at T_N=346 K and an FIM transition at T_C=78 , both with moments aligned in the *ab*-plane. It is shown recently [37] that the AFM order in $ErMn_6Sn_6$ has a spiral character, so that the Mn moments in adjacent layers have an angle relative to each other, and their net moment is canceled by the rare-earth moment, as represented by the arrows at the top of Fig. 2c. In Fig. 2d, $LuMn_6Sn_6$ orders as a collinear in-plane anti-ferromagnet at T_N=415 K and transitions into an AFM flat-spiral structure of ferromagnetic sheets at T_N'=251 K [20]. Note that Lu^{3+} is non-magnetic, hence the absence of a green vector in the caption of Fig. 2d. Our susceptibility data are consistent with previous reports on these materials [18,19].

3.2. Field dependence of magnetization

The field dependence of magnetization is summarized in Fig. 3 for RMn_6Sn_6 with R=Tb, Ho, Er, and Lu. In Figs. 3a and 3b, $TbMn_6Sn_6$ and $HoMn_6Sn_6$ show typical FIM magnetization curves that begin to saturate at approximately 0.2 T when $T \ll T_C$. This transition is of second order as shown by analyzing the Arrott plots in the supplemental Fig. S3.

Unlike $TbMn_6Sn_6$ and $HoMn_6Sn_6$, the magnetization of $ErMn_6Sn_6$ begins to saturate at nearly 1 T, instead of 0.2 T, following a metamagnetic (MM) transition. The MM transition signals a change of magnetic state from AFM to FIM induced by the external magnetic field. Below 1 T, the dark blue $M(H)$ curve in Fig. 2c shows a linear field dependence at $T < T_N$ in $ErMn_6Sn_6$, characteristic of the AFM state. Then at 1 T, a spin-flop transition occurs and magnetization jumps to a higher value. Thus, the $M(H)$ behavior observed in Fig. 3c implies in-plane moments and AFM ordering between the planes at H = 0 followed by a spin-flop (MM transition) at around 1 T in $ErMn_6Sn_6$.

In Fig. 3d, $LuMn_6Sn_6$ shows linear $M(H)$ curves from 0 to 5 T, indicating an AFM ordering. Similar to $LuMn_6Sn_6$, other RMn_6Sn_6 compounds with a non-magnetic rare-earth (R=Y, Sc) show a spiral AFM order [38–40].

3.3. Magnetocaloric effect

We characterized the MCE by evaluating $\Delta S_m(T)$ from the $M(H)$ curves using Eq. (2). The red, green, and blue curves in Fig. 4 trace the change of entropy ($-\Delta S_m(T)$) across the magnetic phase transition under H_{max}=5, 2, and 0.5 T, respectively. The bell-shaped curve for each compound peaks at a temperature near T_C or T_N, where the separation between $M(H)$ curves in Fig. 3 is maximum. It is evident from Eq. (2) that a larger separation between consecutive $M(H)$ isotherms means a larger entropy change. For example, $TbMn_6Sn_6$ and $HoMn_6Sn_6$ show similar $-\Delta S_{MAX}$ values in Figs. 4a, b due to a comparable separation between their magnetization isotherms in Figs. 3a, b.

Despite having comparable $-\Delta S_{MAX}$ values, $HoMn_6Sn_6$ is a more efficient MCM than $TbMn_6Sn_6$ because its bell-shaped $-\Delta S_m(T)$ curve has a larger FWHM. Thus, the refrigerant capacity (RC) defined as the area under the bell-shaped curve within FWHM (Eq. (3)) is greater in $HoMn_6Sn_6$ than in $TbMn_6Sn_6$. The RC values are quoted for each compound in the upper right corner of every panel in Fig. 4. Regardless of H_{max}, the RC values for $HoMn_6Sn_6$ are larger than those for $TbMn_6Sn_6$ due to a larger FWHM.

The significance of FWHM in the MCE is further illustrated in a comparison between $TbMn_6Sn_6$ and $ErMn_6Sn_6$ (Figs. 4a, c). Although $-\Delta S_{MAX}$ in $ErMn_6Sn_6$ is nearly half the value in $TbMn_6Sn_6$ (1.1 vs. 2.3 $JKg^{-1}K^{-1}$), a much larger FWHM (wider bell-shaped curve) produces a larger RC in $ErMn_6Sn_6$ than in $TbMn_6Sn_6$ at H_{max}=5 T (78 vs. 63 JKg^{-1}).

Despite having a larger RC at H_{max}=5 T, $ErMn_6Sn_6$ has a smaller RC than $TbMn_6Sn_6$ at H_{max}=2 and 0.5 T. This is due to the AFM ordering in $ErMn_6Sn_6$ at low fields, which, unlike the FIM state in $TbMn_6Sn_6$, produces a small net magnetization. As shown in Fig. 3c, $ErMn_6Sn_6$ has a linear $M(H)$ curve from zero to 1 T before undergoing the MM

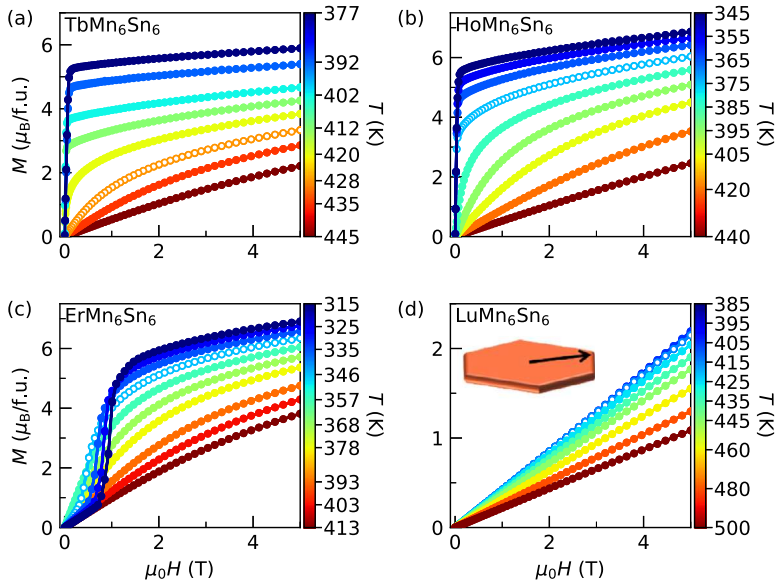

Fig. 3. Field dependence of the magnetization in (a) $TbMn_6Sn_6$, (b) $HoMn_6Sn_6$, (c) $ErMn_6Sn_6$, and (d) $LuMn_6Sn_6$ measured at several temperatures indicated by color bars. All measurements were done with the field in the *ab*-plane as illustrated in the inset of panel d. The temperatures quoted in color bars correspond to the isotherms in each panel. For each compound, the curve with empty symbols is taken at its magnetic transition temperature. (For interpretation of the references to color in this figure legend, the reader is referred to the web version of this article.)

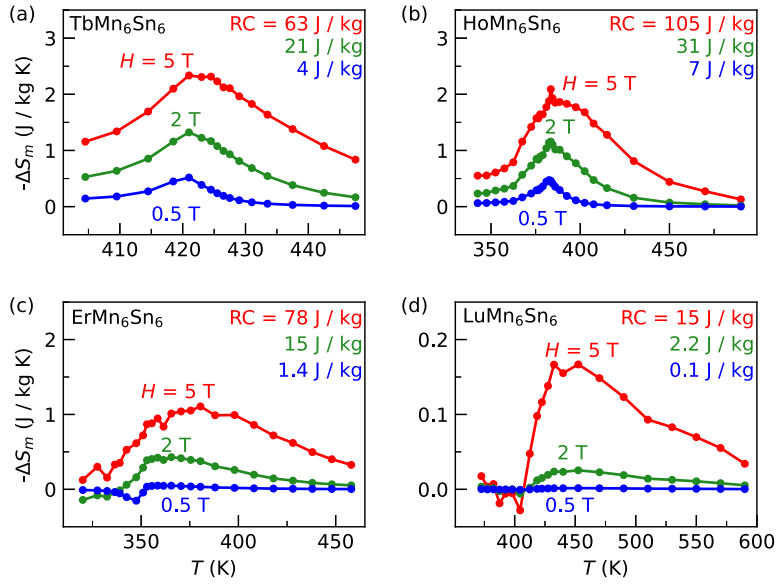

Fig. 4. Magnetocaloric effect evaluated in (a) $TbMn_6Sn_6$, (b) $HoMn_6Sn_6$, (c) $ErMn_6Sn_6$, and (d) $LuMn_6Sn_6$. The red, green, and blue curves correspond to the magnetic entropy integrated with H_{max}=5, 2, and 0.5 T, respectively, according to Eq. (2). All measurements are done with the magnetic field in the *ab*-plane. (For interpretation of the references to color in this figure legend, the reader is referred to the web version of this article.)

transition that changes the shape of its $M(H)$ curves from linear to S-shaped (typical of FIM materials). This field-induced transition from a low-field AFM to a high-field FIM state is responsible for the change of the MCE in $ErMn_6Sn_6$ from small at H_{max}=0.5 T to large at H_{max}=2 and 5 T.

In Fig. 4d, $LuMn_6Sn_6$ shows a very small *RC* even at H_{max}=5 T because it remains in the AFM state from small to large fields. The $M(H)$ curves of $LuMn_6Sn_6$ in Fig. 3d remain linear with minimal separation between consecutive isotherms and without any MM transitions, hence the small MCE at all fields.

3.4. High-entropy forms

High-entropy alloys have recently attracted attention for their ability to increase the MCE [28,29]. The working hypothesis is that the high-entropy alloying procedure randomizes the exchange interactions and broadens magnetic transitions. Therefore, it enhances *RC* due to a larger FWHM according to Eq. (3) [30].

In our study, we decided to examine the effect of creating a high-entropy form of the RMn_6Sn_6 system on the MCE by mixing different rare-earth elements on the *R* site [41]. The EDX map in

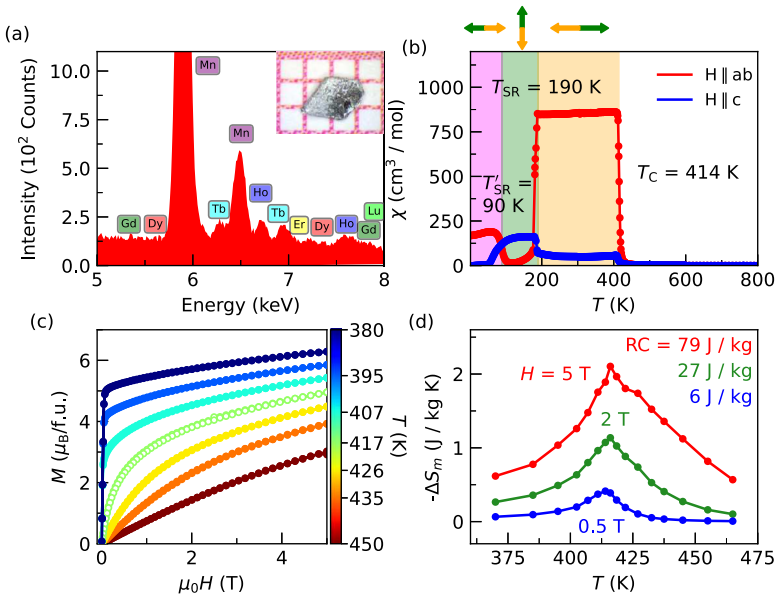

Fig. 5. (a) EDX spectrum confirms the presence of six rare-earth elements in the high-entropy form (6R-HEF). (b) Susceptibility versus temperature shows an FIM transition at high temperatures and two spin reorientation transitions at low temperatures. The green and orange arrows represent the rare-earth and Mn moments, respectively. (c) The Magnetization curves of 6R-HEF. (d) The MCE in the 6R-HEF. All measurements were taken on single crystal samples of 6R-HEF as shown in the inset of (a) with field applied as in the previous single rare-earth materials. (For interpretation of the references to color in this figure legend, the reader is referred to the web version of this article.)

Fig. 5a confirms successful single-crystal growth of the high-entropy form $(Gd_{0.21}Tb_{0.17}Dy_{0.15}Ho_{0.16}Er_{0.19}Lu_{0.13})Mn_6Sn_6$, (see also the supplemental Table S1). We refer to this composition as 6R-HEF. Note that we do not refer to the high-entropy form of RMn_6Sn_6 as a high-entropy alloy, which by definition is not site-specific and contains more than 5 elements each comprising more than 5% of the composition [27]. The susceptibility data in Fig. 5b shows an FIM transition at T_C=414 K followed by spin reorientation transitions at T_{SR}=190 K and T_{SR}'=90 K, respectively. Using $M(H)$ curves near T_C in Fig. 5c, we computed the magnetic entropy change ΔS_m and plotted $-\Delta S_m$ as a function of temperature in Fig. 5d. By integrating the area under the bell-shaped curves, we evaluated RC at H_{max}=5, 2, and 0.5 T. The RC values reported in the inset of Fig. 5d are comparable to those of $TbMn_6Sn_6$ and less than those of $HoMn_6Sn_6$.

The important observation in Fig. 5 is that the MCE in 6R-HEF is not larger than that of the pure RMn_6Sn_6 (compare Fig. 5d and Fig. 4). Similar behavior is seen in high-entropy forms made with fewer rare-earth elements which we discuss in the supplemental material (Figs. S4 and S5). This finding seemingly contradicts the hypothesis that high-entropy alloying randomizes RKKY exchange interactions, broadens the magnetic transition, and increases RC.

The above observation can be explained by noticing that the high-temperature magnetic transition in RMn_6Sn_6 is due to correlations within the Mn kagome sublattice, unlike the low-temperature order which is controlled by the rare-earth sublattice [42]. This can be seen in Figs. 2a and 5b, where the high-temperature T_C (controlled by Mn sublattice) is nearly the same between $TbMn_6Sn_6$ and the 6R-HEF, whereas the low-temperature T_{SR} (controlled by the rare-earth sublattice) is dramatically reduced from 312 K in $TbMn_6Sn_6$ to 190 K in 6R-HEF. Because the high-temperature FIM order is established by correlations within the Mn sublattice, rather than correlations within the rare-earth sublattice, the alloying procedure on the R-site does not enhance the MCE of RMn_6Sn_6.

4. Conclusions

The magnetic ordering of any given RMn_6Sn_6 material depends on the fine balance among three indirect exchange couplings between the Mn layers known as the J_1 (Mn-Sn-Mn), J_2 (Mn-RE-Mn), and J_3 (Mn-Sn-Mn-RE-Mn) couplings [39,42]. In this model, J_1 and J_2 are FM while J_3 is AFM. The relative strength of these interactions, which can be calculated from first principles, determines the ordered state of the material [39,42]. The tunable nature of this J_1–J_2–J_3 model is precisely why the RMn_6Sn_6 compounds are suitable for a comparative study of the MCE. By comparing the MCE metrics among different members of the RMn_6Sn_6 family in Table 1, we draw a few conclusions. (i) FM and FIM transitions (e.g. in $HoMn_6Sn_6$) are more efficient than the AFM transition (e.g. in $LuMn_6Sn_6$) for generating a large MCE. A similar conclusion has been reached by studying the material family R_2BaZnO_5 [9]. (ii) A wide transition, i.e. a large FWHM, is a viable way to increase RC. (iii) We find that creating a high-entropy form by mixing rare-earth elements on the R-site does not enhance the MCE of RMn_6Sn_6 because the high-temperature ordered state is established by correlations within the Mn sublattice instead of R sublattice. For this reason, it is important that future studies of MCE in high-entropy systems mix atoms at a specific site that controls the initial onset of magnetic order.

Table 1
Comparison of MCE metrics with H_{max}=5 T in RMn_6Sn_6 materials investigated in this study. T_c is the higher critical temperature (which could be either FIM or AFM).

Material	T_c (K)	$-\Delta S_{MAX}$ (JKg^{-1}K^{-1})	FWHM (K)	RC (JKg^{-1})
$TbMn_6Sn_6$	428	2.3	36	63
$HoMn_6Sn_6$	375	2.1	57	105
$ErMn_6Sn_6$	346	1.1	89	78
$LuMn_6Sn_6$	415	0.17	112	15
6R-HEF	414	2.1	52	79

CRediT authorship contribution statement

Kyle Fruhling: Writing – review & editing, Writing – original draft, Methodology, Investigation, Formal analysis, Data curation. **Xiaohan Yao:** Formal analysis, Data curation. **Alenna Streeter:** Formal analysis, Data curation. **Fazel Tafti:** Writing – review & editing, Writing – original draft, Supervision, Resources, Project administration, Methodology, Funding acquisition, Conceptualization.

Declaration of competing interest

The authors declare that they have no known competing financial interests or personal relationships that could have appeared to influence the work reported in this paper.

Data availability

Data will be made available on request.

Acknowledgments

The authors acknowledge funding by the National Science Foundation under Award No. DMR-2203512. F.T. and X.Y. acknowledge funding by the Department of Energy, Office of Basic Energy Sciences, Division of Physical Behavior of Materials under award number DE-SC0023124 to perform EDX measurements. The authors thank Z.-C. Wang for the experimental assistance during the early stages of the project.

Appendix A. Supplementary data

Supplementary material related to this article can be found online at https://doi.org/10.1016/j.matchemphys.2024.129230.

References

[1] V.K. Pecharsky, J. Gschneidner, K.A., Giant magnetocaloric effect in $Gd_5Si_2Ge_2$, Phys. Rev. Lett. 78 (23) (1997) 4494–4497, http://dx.doi.org/10.1103/PhysRevLett.78.4494, https://link.aps.org/doi/10.1103/PhysRevLett.78.4494.

[2] B. Yu, M. Liu, P.W. Egolf, A. Kitanovski, A review of magnetic refrigerator and heat pump prototypes built before the year 2010 , Int. J. Refrig. 33 (6) (2010) 1029–1060, http://dx.doi.org/10.1016/j.ijrefrig.2010.04.002, https://www.sciencedirect.com/science/article/pii/S0140700710000721.

[3] A. Alahmer, M. Al-Amayreh, A.O. Mostafa, M. Al-Dabbas, H. Rezk, Magnetic refrigeration design technologies: State of the art and general perspectives, Energies 14 (15) (2021) 4662, http://dx.doi.org/10.3390/en14154662, https://www.mdpi.com/1996-1073/14/15/4662.

[4] N. Terada, H. Mamiya, High-efficiency magnetic refrigeration using holmium, Nature Commun. 12 (1) (2021) 1212, http://dx.doi.org/10.1038/s41467-021-21234-z, https://www.nature.com/articles/s41467-021-21234-z.

[5] X.-M. Luo, Z.-B. Hu, Q.-f. Lin, W. Cheng, J.-P. Cao, C.-H. Cui, H. Mei, Y. Song, Y. Xu, Exploring the performance improvement of magnetocaloric effect based Gd-exclusive cluster Gd_{60}, J. Am. Chem. Soc. 140 (36) (2018) 11219–11222, http://dx.doi.org/10.1021/jacs.8b07841, https://doi.org/10.1021/jacs.8b07841.

[6] K.A. Gschneidner, V.K. Pecharsky, Magnetocaloric materials, Annu. Rev. Mater. Sci. 30 (1) (2000) 387–429, http://dx.doi.org/10.1146/annurev.matsci.30.1.387, https://doi.org/10.1146/annurev.matsci.30.1.387.

[7] V. Franco, J. Blázquez, B. Ingale, A. Conde, The magnetocaloric effect and magnetic refrigeration near room temperature: Materials and models, Annu. Rev. Mater. Res. 42 (1) (2012) 305–342, http://dx.doi.org/10.1146/annurev-matsci-062910-100356, https://doi.org/10.1146/annurev-matsci-062910-100356.

[8] Y. Zhang, Y. Tian, Z. Zhang, Y. Jia, B. Zhang, M. Jiang, J. Wang, Z. Ren, Magnetic properties and giant cryogenic magnetocaloric effect in *B*-site ordered antiferromagnetic Gd_2MgTiO_6 double perovskite oxide, Acta Mater. 226 (2022) 117669, http://dx.doi.org/10.1016/j.actamat.2022.117669, https://www.sciencedirect.com/science/article/pii/S1359645422000544.

[9] P. Xu, L. Hu, Z. Zhang, H. Wang, L. Li, Electronic structure, magnetic properties and magnetocaloric performance in rare earths (RE) based RE_2BaZnO_5 (RE =Gd, Dy, Ho, and Er) compounds, Acta Mater. 236 (2022) 118114, http://dx.doi.org/10.1016/j.actamat.2022.118114, https://www.sciencedirect.com/science/article/pii/S1359645422004955.

[10] Y. Zhang, J. Zhu, S. Li, Z. Zhang, J. Wang, Z. Ren, Magnetic properties and promising magnetocaloric performances in the antiferromagnetic $GdFe_2Si_2$ compound, Sci. Chin. Mater. 65 (5) (2022) 1345–1352, http://dx.doi.org/10.1007/s40843-021-1967-5.

[11] X. Tan, P. Chai, C.M. Thompson, M. Shatruk, Magnetocaloric effect in $AlFe_2B_2$: Toward magnetic refrigerants from earth-abundant elements, J. Am. Chem. Soc. 135 (25) (2013) 9553–9557, http://dx.doi.org/10.1021/ja404107p.

[12] H. Wada, T. Morikawa, K. Taniguchi, T. Shibata, Y. Yamada, Y. Akishige, Giant magnetocaloric effect of $MnAs_{1-x}Sb_x$ in the vicinity of first-order magnetic transition, Physica B 328 (1) (2003) 114–116, http://dx.doi.org/10.1016/S0921-4526(02)01822-7, https://www.sciencedirect.com/science/article/pii/S0921452602018227.

[13] O. Tegus, E. Brück, K.H.J. Buschow, F.R. de Boer, Transition-metal-based magnetic refrigerants for room-temperature applications, Nature 415 (6868) (2002) 150–152, http://dx.doi.org/10.1038/415150a, https://www.nature.com/articles/415150a.

[14] N.J. Jones, H. Ucar, J.J. Ipus, M.E. McHenry, D.E. Laughlin, The effect of distributed exchange parameters on magnetocaloric refrigeration capacity in amorphous and nanocomposite materials, J. Appl. Phys. 111 (7) (2012) 07, http://dx.doi.org/10.1063/1.3679456, https://aip.scitation.org/doi/full/10.1063/1.3679456A334.

[15] H. Ucar, M. Craven, D.E. Laughlin, M.E. McHenry, Effect of Mo addition on structure and magnetocaloric effect in γ-FeNi nanocrystals, J. Electron. Mater. 43 (1) (2014) 137–141, http://dx.doi.org/10.1007/s11664-013-2725-6.

[16] J.S. Amaral, V.S. Amaral, Disorder effects in giant magnetocaloric materials, Phys. Status Solidi (a) 211 (5) (2014) 971–974, http://dx.doi.org/10.1002/pssa.201300749, https://onlinelibrary.wiley.com/doi/abs/10.1002/pssa.201300749.

[17] S.K. Pal, C. Frommen, S. Kumar, B.C. Hauback, H. Fjellvåg, G. Helgesen, Enhancing giant magnetocaloric effect near room temperature by inducing magnetostructural coupling in Cu-doped MnCoGe, Mater. Des. 195 (2020) 109036, http://dx.doi.org/10.1016/j.matdes.2020.109036, https://www.sciencedirect.com/science/article/pii/S0264127520305712.

[18] D.M. Clatterbuck, K.A. Gschneidner, Magnetic properties of RMn_6Sn_6 (R =Tb, Ho, Er, Tm, Lu) single crystals, J. Magn. Magn. Mater. 207 (1) (1999) 78–94, http://dx.doi.org/10.1016/S0304-8853(99)00571-5, https://www.sciencedirect.com/science/article/pii/S0304885399005715.

[19] G. Venturini, B.C.E. Idrissi, B. Malaman, Magnetic properties of RMn_6Sn_6 (R=Sc, Y, Gd-Tm, Lu) compounds with $HfFe_6Ge_6$ type structure, J. Magn. Magn. Mater. 94 (1) (1991) 35–42, http://dx.doi.org/10.1016/0304-8853(91)90108-M, https://www.sciencedirect.com/science/article/pii/030488539190108M.

[20] A. Matsuo, K. Suga, K. Kindo, L. Zhang, E. Brück, K.H.J. Buschow, F.R. d. Boer, C. Lefévre, G. Venturini, Study of the Mn-Mn exchange interactions in single crystals of RMn_6Sn_6 compounds with R =Sc, Y and Lu, J. Alloys Compd. 408–412 (2006) 110–113, http://dx.doi.org/10.1016/j.jallcom.2005.04.080, https://www.sciencedirect.com/science/article/pii/S0925838805005451.

[21] J.-X. Yin, W. Ma, T.A. Cochran, X. Xu, S.S. Zhang, H.-J. Tien, N. Shumiya, G. Cheng, K. Jiang, B. Lian, Z. Song, G. Chang, I. Belopolski, D. Multer, M. Litskevich, Z.-J. Cheng, X.P. Yang, B. Swidler, H. Zhou, H. Lin, T. Neupert, Z. Wang, N. Yao, T.-R. Chang, S. Jia, M. Zahi Hasan, Quantum-limit Chern topological magnetism in $TbMn_6Sn_6$, Nature 583 (7817) (2020) 533–536, http://dx.doi.org/10.1038/s41586-020-2482-7, https://www.nature.com/articles/s41586-020-2482-7.

[22] Z. Li, Q. Yin, Y. Jiang, Z. Zhu, Y. Gao, S. Wang, J. Shen, T. Zhao, J. Cai, H. Lei, S.-Z. Lin, Y. Zhang, B. Shen, Discovery of topological magnetic textures near room temperature in quantum magnet $TbMn_6sn_6$, Adv. Mater. 35 (20) (2023) 2211164, http://dx.doi.org/10.1002/adma.202211164, https://onlinelibrary.wiley.com/doi/abs/10.1002/adma.202211164.

[23] L. Li, M. Yan, Recent progress in the development of $RE_2TMTM'O_6$ double perovskite oxides for cryogenic magnetic refrigeration, J. Mater. Sci. Technol. 136 (2023) 1–12, http://dx.doi.org/10.1016/j.jmst.2022.01.041, https://www.sciencedirect.com/science/article/pii/S1005030222003346.

[24] Y. Zhang, W. Hao, C. Hu, X. Wang, X. Zhang, L. Li, Rare-earth-free $Mn_{30}Fe_{20-x}Cu_xAl_50$ magnetocaloric materials with stable cubic CsCl-type structure for room-temperature refrigeration, Adv. Funct. Mater. 33 (52) (2023) 2310047, http://dx.doi.org/10.1002/adfm.202310047, https://onlinelibrary.wiley.com/doi/abs/10.1002/adfm.202310047.

[25] Y. Zhang, J. Ying, X. Gao, Z. Mo, J. Shen, L. Li, Exploration of the rare-earth cobalt nickel-based magnetocaloric materials for hydrogen liquefaction, J. Mater. Sci. Technol. 159 (2023) 163–169, http://dx.doi.org/10.1016/j.jmst.2023.04.001, https://www.sciencedirect.com/science/article/pii/S1005030223003183.

[26] J.-W. Yeh, S.-K. Chen, S.-J. Lin, J.-Y. Gan, T.-S. Chin, T.-T. Shun, C.-H. Tsau, S.-Y. Chang, Nanostructured high-entropy alloys with multiple principal elements: Novel alloy design concepts and outcomes, Adv. Eng. Mater. 6 (5) (2004) 299–303, http://dx.doi.org/10.1002/adem.200300567, https://onlinelibrary.wiley.com/doi/abs/10.1002/adem.200300567.

[27] E.P. George, D. Raabe, R.O. Ritchie, High-entropy alloys, Nat. Rev. Mater. 4 (8) (2019) 515–534, http://dx.doi.org/10.1038/s41578-019-0121-4, https://www.nature.com/articles/s41578-019-0121-4.

[28] A. Perrin, M. Sorescu, V. Ravi, D.E. Laughlin, M.E. McHenry, Mössbauer analysis of compositional tuning of magnetic exchange interactions in high entropy alloys, AIP Adv. 9 (3) (2019) 035329, http://dx.doi.org/10.1063/1.5079744, https://aip.scitation.org/doi/10.1063/1.5079744.

[29] A. Perrin, M. Sorescu, M.-T. Burton, D.E. Laughlin, M. McHenry, The role of compositional tuning of the distributed exchange on magnetocaloric properties of high-entropy alloys, JOM 69 (11) (2017) 2125–2129, http://dx.doi.org/10.1007/s11837-017-2523-3.

[30] M. Kurniawan, A. Perrin, P. Xu, V. Keylin, M. McHenry, Curie temperature engineering in high entropy alloys for magnetocaloric applications, IEEE Magn. Lett. 7 (2016) 1–5, http://dx.doi.org/10.1109/LMAG.2016.2592462.

[31] J.Y. Law, V. Franco, Pushing the limits of magnetocaloric high-entropy alloys, APL Mater. 9 (8) (2021) 080702, http://dx.doi.org/10.1063/5.0058388.

[32] Y. Zhang, P. Xu, J. Zhu, S. Yan, J. Zhang, L. Li, The emergence of considerable room temperature magnetocaloric performances in the transition metal high-entropy alloys, Mater. Today Phys. 32 (2023) 101031, http://dx.doi.org/10.1016/j.mtphys.2023.101031, https://www.sciencedirect.com/science/article/pii/S2542529323000676.

[33] N. Kinami, K. Wakiya, M. Uehara, J. Gouchi, Y. Uwatoko, I. Umehara, Magnetocaloric effect in single-crystal HoNi with a canted magnetic structure, Japan. J. Appl. Phys. 57 (10) (2018) 103001, http://dx.doi.org/10.7567/JJAP.57.103001, https://iopscience.iop.org/article/10.7567/JJAP.57.103001.

[34] M. Abramchuk, T. Mier, F. Tafti, Tuning the magnetic and structural properties of a three-metal boride alloy: $Mn_{0.95-\delta}Fe_{1.05+\delta-x}Co_xB$, J. Alloys Compd. 805 (2019) 909–914, http://dx.doi.org/10.1016/j.jallcom.2019.07.119, https://www.sciencedirect.com/science/article/pii/S0925838819326167.

[35] B.C. El Idrissi, G. Venturini, B. Malaman, D. Fruchart, Magnetic structures of $TbMn_6Sn_6$ and $HoMn_6Sn_6$ compounds from neutron diffraction study, J. Less Common Metals 175 (1) (1991) 143–154, http://dx.doi.org/10.1016/0022-5088(91)90359-C, https://www.sciencedirect.com/science/article/pii/002250889190359C.

[36] B. Malaman, G. Venturini, R. Welter, J.P. Sanchez, P. Vulliet, E. Ressouche, Magnetic properties of RMn_6Sn_6 (R=Gd-Er) compounds from neutron diffraction and Mössbauer measurements, J. Magn. Magn. Mater. 202 (2) (1999) 519–534, http://dx.doi.org/10.1016/S0304-8853(99)00300-5, https://www.sciencedirect.com/science/article/pii/S0304885399003005.

[37] Simon X.M. Riberolles, Tianxiong Han, Tyler J. Slade, J.M. Wilde, A. Sapkota, Wei Tian, Qiang Zhang, D.L. Abernathy, L.D. Sanjeewa, S.L. Bud'ko, P.C. Canfield, R.J. McQueeney, B.G. Ueland, New insight into tuning magnetic phases of rmn6sn6 kagome metals, 2023, Submitted for publication https://arxiv.org/abs/2306.13206.

[38] G. Venturini, D. Fruchart, B. Malaman, Incommensurate magnetic structures of RMn_6Sn_6 (R = Sc, Y, Lu) compounds from neutron diffraction study, J. Alloys Compd. 236 (1) (1996) 102–110, http://dx.doi.org/10.1016/0925-8388(95)01998-7, https://www.sciencedirect.com/science/article/pii/0925838895019987.

[39] N.J. Ghimire, R.L. Dally, L. Poudel, D.C. Jones, D. Michel, N.T. Magar, M. Bleuel, M.A. McGuire, J.S. Jiang, J.F. Mitchell, J.W. Lynn, I.I. Mazin, Competing magnetic phases and fluctuation-driven scalar spin chirality in the kagome metal YMn_6Sn_6, Sci. Adv. 6 (51) (2020) eabe2680, http://dx.doi.org/10.1126/sciadv.abe2680, https://www.science.org/doi/full/10.1126/sciadv.abe2680.

[40] H. Zhang, C. Liu, Y. Zhang, Z. Hou, X. Fu, X. Zhang, X. Gao, J. Liu, Magnetic field-induced nontrivial spin chirality and large topological hall effect in kagome magnet $ScMn_6Sn_6$, Appl. Phys. Lett. 121 (20) (2022) 202401, http://dx.doi.org/10.1063/5.0127091.

[41] L. Min, M. Sretenovic, T.W. Heitmann, T.W. Valentine, R. Zu, V. Gopalan, C.M. Rost, X. Ke, Z. Mao, A topological kagome magnet in high entropy form, Commun. Phys. 5 (1) (2022) 1–7, http://dx.doi.org/10.1038/s42005-022-00842-1, https://www.nature.com/articles/s42005-022-00842-1.

[42] Y. Lee, R. Skomski, X. Wang, P.P. Orth, Y. Ren, B. Kang, A.K. Pathak, A. Kutepov, B.N. Harmon, R.J. McQueeney, I.I. Mazin, L. Ke, Interplay between magnetism and band topology in kagome magnets RMn_6Sn_6, Phys. Rev. B 108 (4) (2023) 045132, http://dx.doi.org/10.1103/PhysRevB.108.045132, https://journals.aps.org/prb/abstract/10.1103/PhysRevB.108.045132.